ACS APPLIED MATERIALS & INTERFACES

Research Article

www.acsami.org

Impact of Silicon Nanocrystal Oxidation on the Nonmetallic Growth of Carbon Nanotubes

Conor Rocks,*[,†] Somak Mitra,[†] Manuel Macias-Montero,[†] Paul Maguire,[†] Vladimir Svrcek,[‡] Igor Levchenko,[§] Kostya Ostrikov,[§,∥] and Davide Mariotti*[,†]

[†]Nanotechnology & Integrated Bio-Engineering Centre (NIBEC), Ulster University, Coleraine, Londonderry BT52 1SA, United Kingdom

[‡]Research Center for Photovoltaics, National Institute of Advanced Industrial Science and Technology (AIST), Central 2, Umezono 1-1-1, Tsukuba 305-8568, Japan

[§]School of Chemistry, Physics, and Mechanical Engineering, Queensland University of Technology, Brisbane, Queensland 4000, Australia

[∥]Joint CSIRO−QUT Sustainable Materials and Devices Laboratory, CSIRO, P.O. Box 218, Lindfield, New South Wales 2070, Australia

Supporting Information

ABSTRACT: Carbon nanotube (CNT) growth has been demonstrated recently using a number of nonmetallic semiconducting and metal oxide nanoparticles, opening up pathways for direct CNT synthesis from a number of more desirable templates without the need for metallic catalysts. However, CNT growth mechanisms using these nonconventional catalysts has been shown to largely differ and reamins a challenging synthesis route. In this contribution we show CNT growth from partially oxidized silicon nanocrystals (Si NCs) that exhibit quantum confinement effects using a microwave plasma enhanced chemical vapor deposition (PECVD) method. On the basis of solvent and a postsynthesis frgamentation process, we show that oxidation of our Si NCs can be easily controlled. We determine experimentally and explain with theoretical simulations that the Si NCs morphology together with a necessary shell oxide of ∼1 nm is vital to allow for the nonmetallic growth of CNTs. On the basis of chemical analysis post-CNT-growth, we give insight into possible mechanisms for CNT nucleation and growth from our partially oxidized Si NCs. This contribution is of significant importance to the improvement of nonmetallic catalysts for CNT growth and the development of Si NC/CNT interfaces.

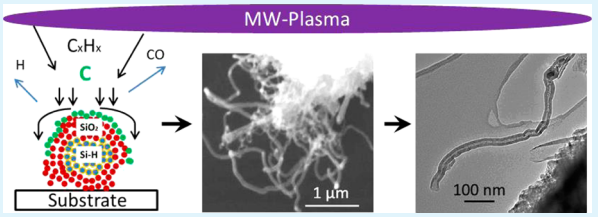

KEYWORDS: *silicon nanocrystals, carbon nanotubes, nonmetallic catalyst, plasma, nanocomposite*

INTRODUCTION

Two of the most environmentally friendly and abundant elements are carbon (C) and silicon (Si). It is therefore no coincidence that they play important and fundamental roles in numerous technologies. In recent decades, new opportunities have become viable due to the unique properties that are exhibited by nanosized C and Si. The use of Si within many optoelectronic devices has been limited by the indirect bandgap nature of bulk silicon, which presents poor absorption and emission properties. However, once Si nanocrystals (Si NCs) are synthesized with diameters that are comparable to or below the Bohr radius (<5 nm), a widening of the energy bandgap is observed, leading to novel optoelectronic properties.[1] Consequently, the radiative recombination processes can be altered on the basis of the Si NCs diameter. Additionally, at these dimensions, nanocrystals are considerably affected by their high surface to volume ratio, meaning that the Si NCs surface chemistry can strongly impact the overall behavior and properties.[2] However, the enhanced optoelectronic properties, small size, and increased curvature of these nanocrystals can be highly benifical for a variety of applications that include bioimaging, drug delivery, solar cells, and LEDs.[3,4] Similar to Si NCs, C nanomaterials have also been extensively studied by the scientific community in recent decades.[5−7] Popular industrial processes such as chemical vapor deposition and pyrolysis can be used to synthesize complex and functional C nanoarchitectures such as carbon nanotubes (CNTs), graphene, and fullerenes[5,8,9] These C structures based on sp^2 hybridization have gained attention due to their high strength/stiffness, low density, and high electrical/thermal conductivities.[10] CNTs in particular have been the focus of many research groups because of their versatility in design (chirality, single-walled, multiwalled), enabling fine-tuning of their unique properties that are promising for many future applications.[11−14]

Still, the growth of high-quality CNTs often relies on metal catalyst particles that remain within CNTs after synthesis and

Received: March 1, 2016
Accepted: June 30, 2016
Published: June 30, 2016

DOI: 10.1021/acsami.6b02599
ACS Appl. Mater. Interfaces 2016, 8, 19012−19023

can affect their implementation into numerous applications. A number of post-treatment techniques have been established to purify the CNTs of remaining impurities.[15,16] Nevertheless, these postgrowth techniques add complexity and are not benifical for rapid, low-cost production. The possibilty to grow CNTs on desired substrates or templates through the use of a nonmetallic catalyst is a highly desired solution. CNT growth has previously been demonstrated on a number of nonmetallic semiconducting and metal oxides nanoparticles to produce single- and double-walled nanotubes.[8,17] For instance, the growth on metal oxide nanoparticles has been shown to differ drammatically from CNT growth on metal catalysts, where different types of growth mechanisms have been identified.[18] Of particular importance is the possibility of using silicon to catalyze CNT growth because of the potential to implement directly into a number of highly established Si-based technologies. Futhermore, with tunable optical and electronic properties that Si NCs and CNTs display, the possibility of coupling Si NCs and CNTs to produce innovative devices and/or components at the nanoscale is a very attractive opportunity. Si NCs/CNTs nanostructures present new possibilities to explore nano device architectures that will lead to innovative and improved design approaches. In principle, a SiNC/CNT system would present an almost perfect optoelectronic nanocomponent, creating an interface between two quantum confined nanostructures, where the possibility of multiple exctions generated by the Si NCs can be coupled with CNTs to enhance exciton dissociation and charge transport. There are a number of applications that could benefit from the operation of such a Si NC/CNT nanojunction. For example, the high volumetric along with large gravimetric capacities of Si[20] are attrative characteristics that can be combined with CNTs for numerous energy applications. The inclusion of CNTs could improve the mechanical stability as well as enhancing charging and discharging speeds. The improved performance of a CNT/Si composite for energy storage, specifically high reverse capacity of more than 3000 A h g^{-1}, was validated by a number of groups.[20,21] Lately, Si NCs have been shown to act as an ideal photocatalyst to reduce CO_2 in aqueous environments.[22,23] Introducting a Si NC/CNT photocatalyst would present increased surface areas as well as more efficient charge separation and transport, enhancing the overall performance and reduction of CO_2 species. In some instances, the fabrication of Si NC/CNT composites has been accomplished using simple solution chemistry methods, where we have successfully encapsulated Si NCs within the CNT cavities.[24] Furthermore, an electrostatic force process has been shown to be somewhat effective in attaching Si NCs to the outer walls of CNTs.[24] However, it is very likely that the Si NC/nanocarbon structures promoted using the above techniques rely on weak chemical interactions essentially achieved postsynthesis, meaning that subsequent optical and electronic coupling between the Si NCs and CNTs would undoubtedly suffer. Therefore, the possibility to directly grow CNTs from Si NCs, forming a chemically attached Si NC/CNT junction, is a very intereasting and exciting prospect. Direct CNT growth using Si NCs as a catalyst may be accomplished through management of the nanocrystals surface characteristics where, on the basis of our previous work, oxygen appears to play a key role for successful growth.[19,24] Oxygen coordination at the Si NCs surface may influence chemical bonding with the CNT, although careful control over the oxide thickness is required in order for the Si NCs to maintain their desired optoelectronic properties after CNT growth.

In our previous work CNT growth was attempted using a CH_4 low-pressure plasma treatment directly from Si NCs that had been processed by different methods.[19,25] Low yields of CNTs were grown from electrochemically etched Si NCs, suggesting that particle size and the extent of the surface oxide played a vital role in the successful growth of CNTs from nonmetallic Si NCs. However, we were unable to understand the role of oxide on CNT growth. Through a more in depth, systematic experimental and theoretical study we have now been able to identify key features on the Si NCs surfaces, overcoming previous challenges. Our detailed and quantitative analysis allowed us to provide a clear insight into mechanisms for CNT growth from nonmetallic Si NCs.

We demonstrate in this study the synthesis and production of a nanoscale composite of Si NCs/CNTs using a microwave plasma-enhanced chemical vapor deposition (PECVD) process. We establish a procedure for controlled oxide growth based on solvent and a fragmentation process that presents the required Si NC morphology and surface characteristics for successful CNT nucleation. Our experimental measurements enable us to determine that a threshold oxide thickness of ∼1 nm is necessary before CNT growth can occur from our nonmetallic Si NCs catalysts.

RESULTS

Sample Description and Oxidation Procedure. Si NCs are produced here from porous silicon following an established electrochemical etching procedure (see Experimental Section below). After mechanical pulverization, porous silicon yields a powder made up of agglomerates (up to micrometers in size) of Si NCs with diameters in the range 2−3 nm (Figure 1a). The

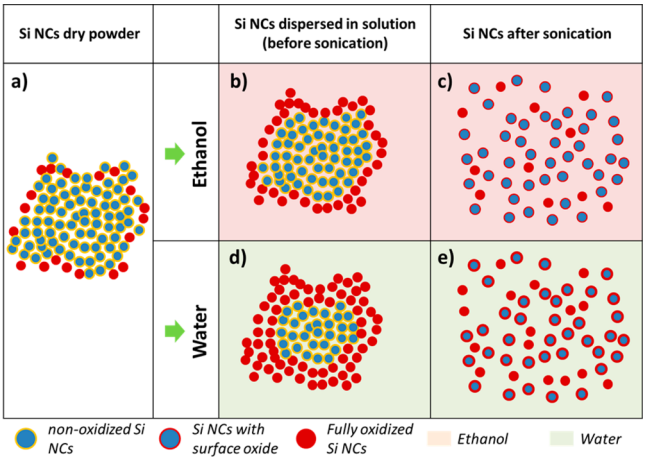

Figure 1. Schematic representation of (a) as-prepared agglomerated silicon nanocrystals, (b) as-prepared silicon nanocrystals in ethanol, (c) fragmented silicon nanocrystals in ethanol following sonication, (d) as prepared silicon nanocrystals in deionized (DI) water, and (e) fragmented silicon nanocrystals in DI water following sonication.

Si NCs at the surface of the large agglomerates tend to be oxidized; however, interfaces between Si NCs within the agglomerates are not oxidized but hydrogen terminated, possibly with surface defects and dangling bonds.[26] Therefore, only the Si NCs on the superficial layers of the agglomerates are affected by oxidation, whereas the SiNCs found within the agglomerates are somewhat protected and remain unexposed to

DOI: 10.1021/acsami.6b02599
ACS Appl. Mater. Interfaces 2016, 8, 19012−19023

oxidizing species. When the agglomerates are dispersed in water or ethanol, the superficial Si NCs will be subject to further oxidation (Figure 1b,d). However, sonication of the samples in water or in ethanol promotes the fragmentation of the Si NCs agglomerates, whereby exposure of the inner Si NCs interfaces induces oxidation on most of the Si NCs (Figure 1c,e). We therefore use the sonication process for different periods and in different solutions to achieve different degrees of controlled oxidation, namely, slower in ethanol (Figure 1b,c) and faster in water (Figure 1d,e). The detailed chemical analysis confirming the oxidation states as described here will be provided further below. Following the oxidation procedure, Si NCs with varying oxidation states will be used as CNT growth catalysts to evaluate the impact of the Si NCs oxidized surface on the growth mechanisms.

Chemical Analysis of Si NCs Prior to CNT Growth. Previous results have indicated oxide growth on Si NCs follwing a sonication process in both DI water and ethanol.[19] Additional measurements and a more detailed analysis that includes deconvolution of the oxide peaks, including doublets, and suboxide peaks has confirmed the formation of differet oxide arrangements on the Si NCs surface (Figures 2 and 3). X-ray photoelectron spectroscopy (XPS) investigation into the Si 2p area for our Si NCs prepared in deionized (DI) water and following subsequent sonication times was performed (Figure 2). XPS spectra were calibrated to 284.8 eV according to the C 1s core level binding energy (BE).[27] Si 2p core-level spectra were fitted using Gaussian line shapes after linear background subtraction. For the $2p_{3/2}$–$2p_{1/2}$ doublet, the intensity ratio of 2:1 and constant splitting of 0.61 eV was taken into account. The Si 2p spectrum is commonly acknowledged as a superposition of five peaks that correspond to the Si 2p core levels of Si^0 and each of the individual $Si–O_n$ bonding arrangements in the amorphous SiO_x layer and where $n = 1–4$ represents the oxidation states Si_2O (Si^{1+}), SiO (Si^{2+}), Si_2O_3 (Si^{3+}), and SiO_2 (Si^{4+}). The BEs relative to the Si^0 position for each Si $2p_{3/2}$ suboxide components are 0.95, 1.57, 2.56, and 3.82 eV, respectively. After deconvolution of the XPS spectra the metallic Si^0 peak, typically found around 99.7 eV,[28] was absent for Si NCs dispersed in DI water (Figure 2a). The XPS measurement in this case (Figure 2a) assesses the chemical composition of highly agglomerated nanocrystals forming large micrometer-sized structures (Figure 1a). The non-appearance of a metallic Si^0 peak for Si NCs as-prepared in DI water (Figure 2a) is essentially because the superficial Si NCs are

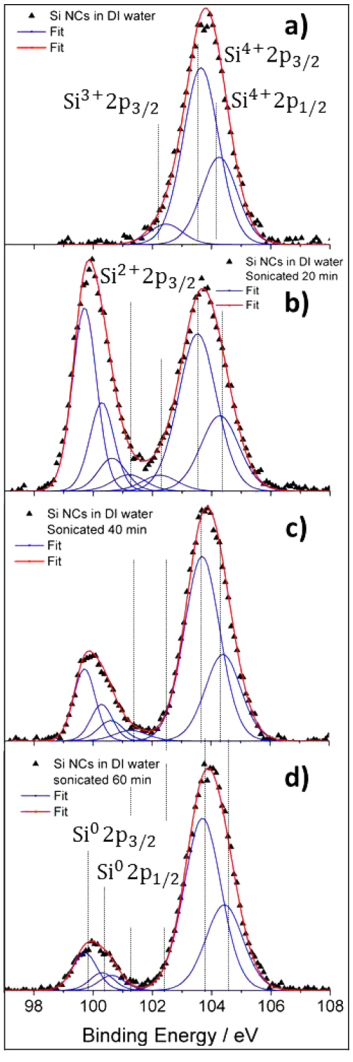

Figure 2. (a) X-ray photoelectron spectra for as-prepared silicon nanocrystals (Si NCs) in deionized (DI) water and (b–d) after different sonication times: (b) 20 min, (c) 40 min and (d) 60 min.

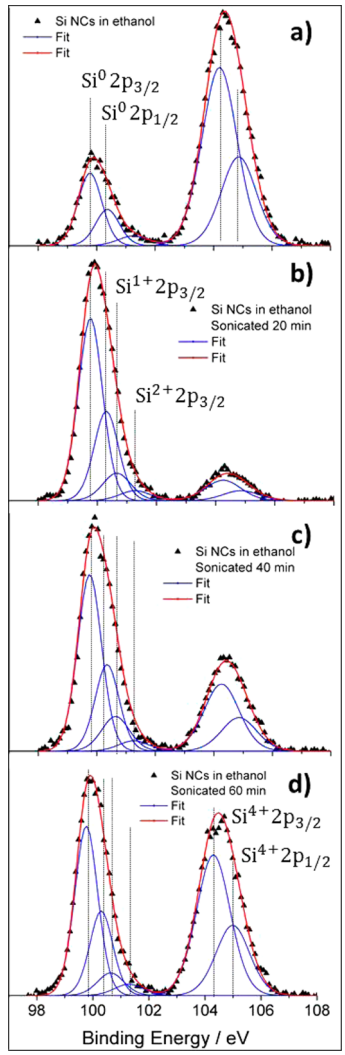

Figure 3. (a) X-ray photoelectron spectra for silicon nanocrystals (Si NCs) prepared in ethanol and (b–d) after different sonication periods: (b) 20 min, (c) 40 min, and (d) 60 min.

DOI: 10.1021/acsami.6b02599
ACS Appl. Mater. Interfaces 2016, 8, 19012–19023

extensively (or fully) oxidized and form an oxide layer all around each agglomerate (red contour in Figure 1d). The penetration depth of the X-ray source (~10 nm) is less than the accumulated thickness of these oxidized agglomerates and therefore does not detect Si−Si bonds.

After 20 min sonication in DI water, the metallic Si^0 peak positioned at 99.7 eV is easily observed (Figure 2b). The sonication process has encouraged the breaking up of agglomerates with heavily oxidized Si NCs at the surface, uncovering new Si−Si bonds of the inner Si NCs, which were not exposed to oxidizing species (Figure 1e).

Following the fragmentation of large agglomerates, the Si^0 intensity is observed to decrease following an increase in sonication time (40 and 60 min, Figure 2c,d respectively). The assumption can then be made that because of this sequential reduction in Si^0 intensity with continued sonication time the bulk of large agglomerates have been effectively fragmented and fragmented Si NCs are being oxidized at their surface (Figure 1e). Similarly, XPS analysis was performed for Si NCs prepared in ethanol and following subsequent sonication time periods (Figure 3).

Oxidation of the Si NCs at the surface of non-fragmented agglomerates in ethanol (Figure 1b) is slower than in water. For this reason XPS measurements still exhibit the metallic Si^0 peak (Figure 3a), which was completely absent in the corresponding XPS measurements of the agglomerates in water (Figures 2a and 1d). Following 20 min of sonication, large oxidized agglomerates have been fragmented to expose new Si−Si bonds (Figure 1c) showing an intense Si^0 peak and negligible oxidation components (Figure 3b). Further sonication time (40 and 60 min, Figure 3c,d, respectively) shows that oxidation advances at a reduced rate in comparison to Si NCs that were sonicated in DI water (Figure 2c,d). Fourier transform infrared spectroscopy (FTIR) for Si NCs in ethanol and DI water showed characteristic Si−O−Si and Si−H bending and stretching modes that has been covered extensively in earlier works by our group and are reported for convenience in the Supporting Information.[29,19] The relative increase in ratio of the FTIR transmittance peaks at 1100 and 2100 cm^{-1} were analyzed (Figure 4a) and correspond to Si−O−Si and Si−H stretching modes, respectively.[30,31] We observe that the sonication process clearly accelerates the replacement of Si−H bonds in both ethanol and DI water, the latter proceeding at an increased rate as consistently highlighted (Figure 2 and 3). Because of the much larger penetration depth (μm) from the infrared laser compared to XPS energy source, Si−H stretching peak can be detected for Si NCs prepared in DI water. This further confirms the XPS analysis and our description of the oxidation process for Si NCs prepared in ethanol/DI water and during sonication intervals. Furthermore, XPS measurements give us the opportunity to quantify the oxidation degree and link this to the subsequent CNT growth.

Quantification of the Oxide Growth on Si NCs Samples. We evaluated the oxide thickness (T_{ox}) and plotted it against the sonication time for Si NCs ethanol and DI water, where T_{ox} was quantified (Figure 4b) on the basis of deconvoluted XPS spectra of Figures 2 and 3 and determined with the following expression:[32]

$$T_{ox} = L_{SiO_2} \sin\theta \ln\left[\left(\frac{I_{Si}^{\infty}}{I_{SiO_2}^{\infty}}\frac{I_{SiO_2}}{I_{Si}}\right) + 1\right] \quad (1)$$

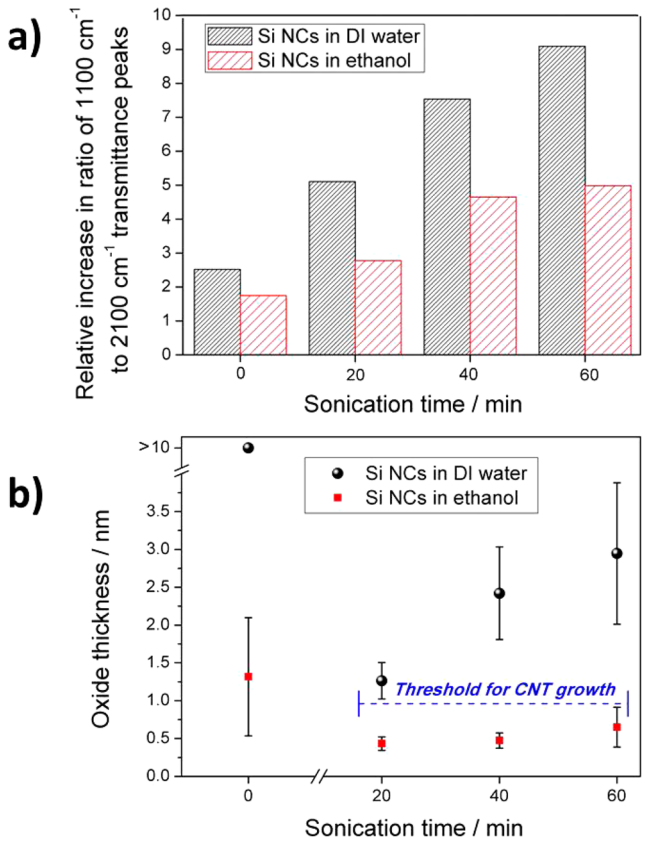

Figure 4. (a) Graph depicting the ratio between 1100 and 2100 cm^{-1} FTIR absorption peaks for silicon nanocrystals (Si NCs) prepared in ethanol/deionized (DI) water and after subsequent sonication time periods. (b) Oxide thickness calculation using fitted X-ray photoelectron spectral data Si NCs prepared in ethanol/DI water and following sonication time periods.

The attenuation length (L_{SiO_2}) of 3.485 nm (ISO/DIS 14701 standard) for photoelectrons (Si 2p) in SiO_2 was used. I_{Si} and I_{SiO_x} represent the intensity of nonoxidized and oxidized Si. I_{SiO_x} was determined by considering the quantity of Si in each suboxide population I_{Si}^{1+}, I_{Si}^{2+}, I_{Si}^{3+}, and I_{Si}^{4+} relative to virtually pure Si^{4+}:

$$I_{SiO_x} = 0.25I_{Si^{1+}} + 0.5I_{Si^{2+}} + 0.75I_{Si^{3+}} + I_{Si^{4+}} \quad (2)$$

The ratio $I_{Si}^{\infty}/I_{SiO_2}^{\infty}$ is a constant that compares the intensities of "infinitely" thick Si^0 and SiO_2 and is equal to 0.9329 (ISO/DIS 14701 standard). θ is 58° and is the angle of the electron analyzer and the sample surface. The analytical method described above is typically used for samples that are planar and not with spherical shapes, which results in a largely overestimated oxide thickness. However, the shape can be taken into consideration by introducing a geometric factor, which in our case results to be equal to $^1/_2$.[33]

By using this analytical technique we obtain absolute values, highlighting the modified rate of oxidation for Si NCs in each solvent as a consequence of the sonication process (Figure 4b). We observe for our agglomerated Si NCs prepared in ethanol T_{ox} values of 1.31 ± 0.78 nm. No metallic Si^0 peak was observed from our XPS analysis of Si NCs prepared in DI-water (Figure 2a), so we are unable to apply the analytical model to obtain a value for T_{ox}. However, we know that the penetration depth of our Al X-ray source ($h\nu$ = 1486.6 eV) is ~10 nm, so

DOI: 10.1021/acsami.6b02599
ACS Appl. Mater. Interfaces 2016, 8, 19012−19023

we can assume a value of T_{ox} > 10 nm in this case. The thickness of as-parepared samples (left side, Figure 4b) has to be attributed to the oxidation of Si NCs at the surface of the agglomerates only (Figure 1b,d); therefore in the case of the samples dispersed in water, the measurements and model suggest that 3−4 superfical Si NCs layers are fully oxidized (if we remember that Si NCs have a 2−3 nm diameter). After 20 min of sonication in ethanol and DI-water, the model produces T_{ox} values of 0.43 ± 0.08 nm and 1.26 ± 0.22 nm, respectively. Because the sonication process has successfully fragmented the large agglomerates into smaller or single Si NC arrangements, these values can be predominantly attributed to the actual oxidation degree of Si NCs and not the Si NCs at the surface of the agglomerates only. Continued sonication (40 and 60 min) contributes to further oxidation of the Si NCs with an increasing oxide thickness. Both oxide thickness and rate of oxidation are much more pronounced in water than in ethanol, confirming the oxidizing role of water molecules. We also observe changes in the rate of oxidation with sonication time, which are more easily seen in the samples that were sonicated in water.

It should be noted here that the oxidation rate can vary, and among other factors, it depends also on the agglomerate size and indeed on the thickness of the existing oxide layer. Initially, the agglomerate size influences the degree of coverage of adsorbed species on its surface. The surface density of hydroxyl and water molecules is generally lower for smaller particles due to varying particle curvature.[34,35] As a consequence, in the early stages and for large agglomerates, oxidizing molecules are found at a higher degree of surface density thus contributing to a more rapid oxidation. At the same time, Si NCs present an increased surface area with higher reactivity due to the presence of high-energy surface features that may speed up the oxidation process. It follows that the rate of oxidation in the initial stages is the result of competing mechanisms and that surface reaction rates and density of oxidizing species are the limiting factors. Nonetheless, in the following stages during inward oxide growth, the oxidation rate in Si NCs is drastically slowed down due to geometrial and mechanical constraints.[36,37] The continued growth of the oxide results in diffusion limited growth because the oxidizing species are expected to diffuse through the already thick oxide layer in order to reach the Si−SiO_2 interface. This typically results in parabolic growth rate due to the oxide growth being proportional to the square root of the oxidation time.[38]

In the case of our Si NCs sonicated in ethanol, we observe a slow monotonic trend and increasing oxide thickness due to the lower water content coupled with a reduced oxidation rate for small Si NCs. However, we observe that for our Si NCs sonicated in DI-water, oxidation expectedly proceeds at an increased rate in comparison to Si NCs sonicated in ethanol. Furthermore, the rate of oxidation appears to be clearly reduced after 40 min sonication; it is possible that T_{ox} is approaching a maximum value and the reaction has become diffusion limited in this case.

Characterization of Si NCs/CNTs Following the CNT Growth Process. Si NCs with varying oxidation states were then drop cast on substrates and subjected to a PECVD process to grow CNTs (see Experimental Section). Scanning electron microscopy (SEM) of all samples post plasma treatment was performed. SEM of Si NCs sonicated in DI water after plasma treatment showed the appearance of CNT structures (Figure 5a−c). The formation of unorganized fibrous arrangements

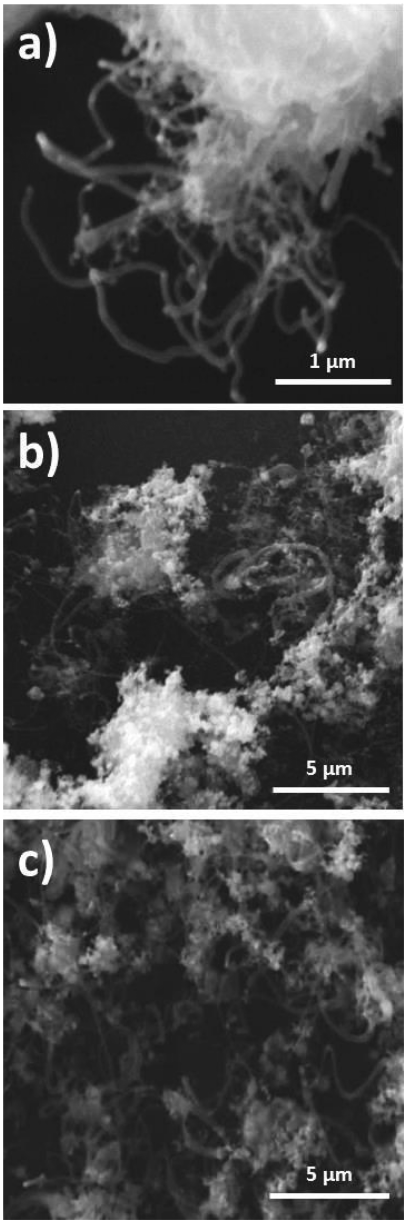

Figure 5. Carbon nanotubes grown from silicon nanocrystals in deionized water and sonicated for (a) 20 min, (b) 40 min, and (c) 60 min.

with lengths up to 5 μm were found for each sonication interval (20, 40, and 60 min). This was particularly detected for Si NCs that were sonicated for 60 min in DI water. It is important to highlight that CNT nucleation and growth from Si NCs prepared in DI water or for Si NCs prepared and sonicated in ethanol was not possible; therefore, further characerization within this section is performed and discussed only for samples with Si NCs sonicated in DI water for 20, 40, and 60 min which were successful in catalyzing CNT growth.

Because the growth of CNTs is only achieved using Si NCs in DI water that had been fragmented using a sonication process, the following comments can be made: (a) Si NCs prepared in DI water and ethanol contain large agglomerates that are not of appropriate dimensions or morphology for successful nucleation of CNTs. (b) An oxide thickness (as highlighted in Figure 4b) below a certain threshold (<1 nm) prevents Si NCs from acting as a suitable catalyst. Detailed

DOI: 10.1021/acsami.6b02599
ACS Appl. Mater. Interfaces 2016, 8, 19012−19023

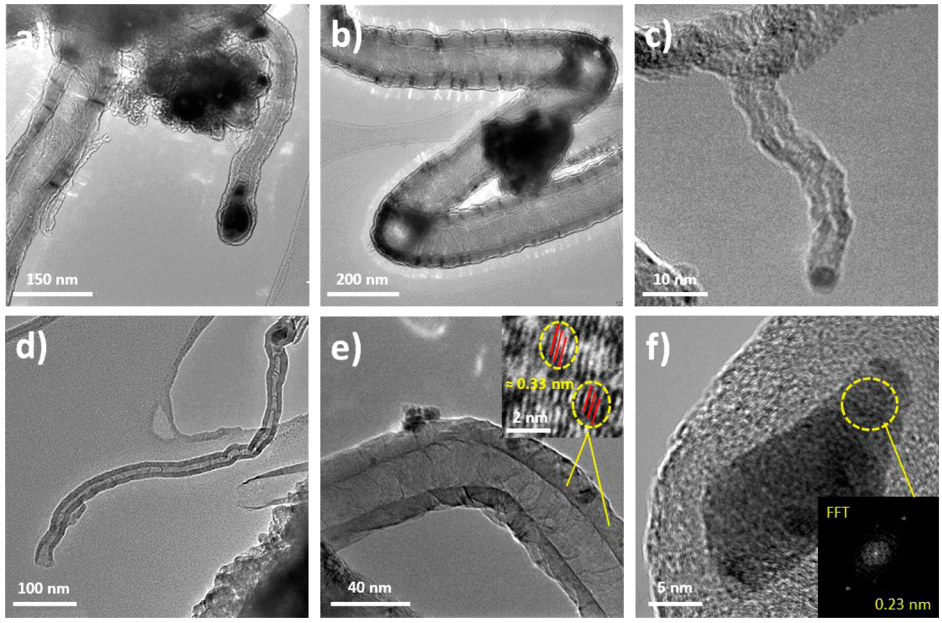

Figure 6. (a–c) Transmission electron microscopy images of carbon nanotubes grown from silicon nanocrystals in deionized water sonicated for 60 min using a microwave plasma chemical vapor deposition process.

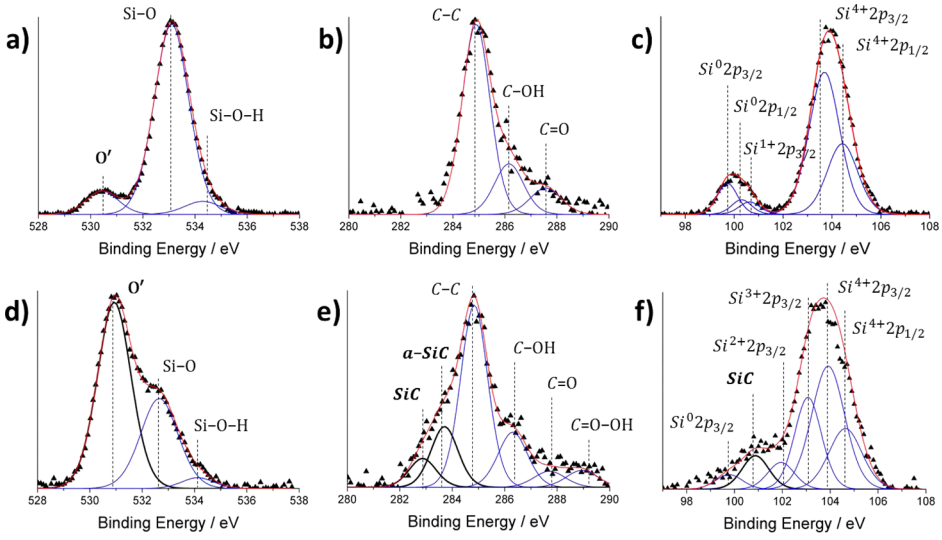

Figure 7. X-ray photoelectron spectroscopy analysis of O 1s, C 1s, and Si 2p regions for (a–c) oxidized Si nanocrystals (NCs) before the plasma process (60 min sonication in DI water) and (d–f) after carbon nanotube growth. Panel c corresponds to Figure 2d and is reproduced here to ease the comparison.

transmission electron microscope (TEM) images of CNTs that have been grown using oxidized Si NCs (60 min sonication in DI water) as a nonmetallic catalyst were obtained. The nanotubes produced are of varying diameters and sizes (Figure 6a–d), originating mainly from Si NC agglomerates that range in dimensions as well as from a single nanocrystal (Figure 6c).

The detailed TEM analysis (Figure 6e) has shown that CNTs are multiwalled in nature with up to 15 layers. The measured spacing of ~0.33 nm between each of the layers correlates with the *d*-spacing associated with the (002) plane of graphite. It is predicted from the condensed array of unorganized nanotubes that CNTs have precipitated outward from the end of our Si NCs and hence are removed from the substrate (tip-growth). Nanotubes are seen to grow directly from small agglomerates (i.e., much smaller than as-prepared micrometer-sized agglomerates) of oxidized Si NCs with the fast Fourier transform image showing (102) *d*-spacing of 0.23 nm for SiO_2 (Figure 6f).

Additionally, Raman spectroscopy was used to characterize our Si NCs/CNTs composite post PECVD process (see Supporting Information). We observe both D, G, and 2D bands typical of graphitic structures. The intense D band observed suggests our grown CNTs are highly defective, which is typical in multiwalled structures. At the same time carbon deposits may be present across each sample that did not catalyze due to the nonuniformity of the catalyst layer. This is confirmed by the 2D region (second-order phonon process), which also shows numerous low intense peaks in the range 2400–3000 cm^{-1}, characteristic of multilayered amorphous structures. Because the investigation is still fundamental in nature, we expect that an optimization process will be able to lead to improved growth yields and higher quality of the CNTs. Further chemical

DOI: 10.1021/acsami.6b02599
ACS Appl. Mater. Interfaces 2016, 8, 19012–19023

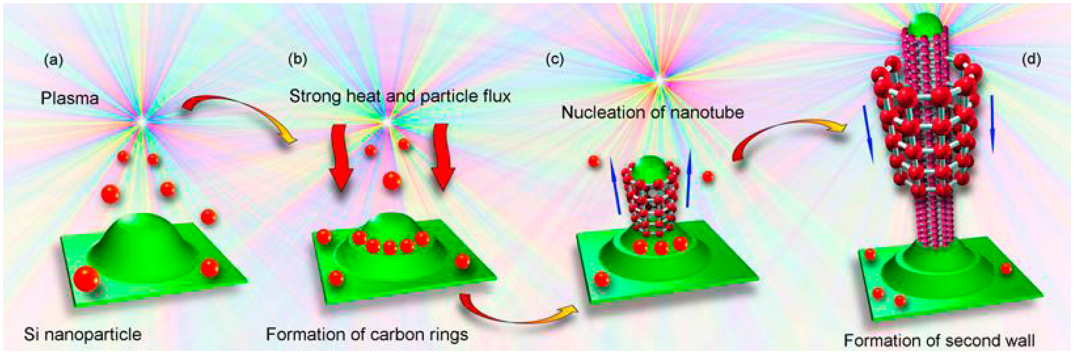

Figure 8. Plausible scenario of the nucleation and growth of carbon nanotube from silicon nanocrystal in reactive plasma environment. The silicon nanocrystals dispersed on the surface subjected to plasma treatment (a) resulted in heating and possibly reshaping of the nanocrystals. Next, the carbon chains were formed on the surface features of nanocrystals (b) and finally the tip-growth of the nanotube was started (under continuing plasma effect) (c). The growth proceeded by nucleating and extruding the next layers over already formed (d). Finally, the multiwalled carbon nanotube was formed, with the oxidized silicon nanocrystal been captured in the nanotube tip.

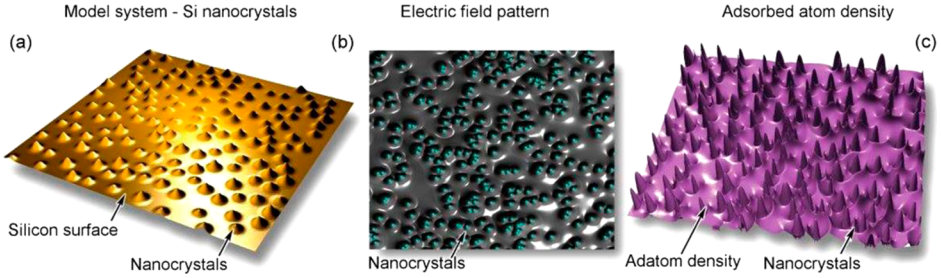

Figure 9. Numerical simulation of the main processes involved in carbon nanotube nucleation and growth from silicon nanocrystals in plasma. (a) Model system consisting of small (10−50 nm) nanocrystals on silicon surface. (b) Calculated electric field pattern in the model system demonstrates strong field strength near nanocrystals. (c) Calculated pattern of adsorbed atom density in the model system shows high density between the nanocrystals and low density near nanocrystal surfaces, as a signature of strong fluxes from the surface to nanocrystals.

characterization of the samples postgrowth was also carried out by XPS (Figure 7).

Figure 7 shows the XPS anaylsis of our oxidized Si NCs in water before (Figure 7a−c) and after (Figure 7d−f) our PECVD process. The O 1s spectrum (Figure 7a) is comprised of peaks located around 530.5, 533.0, and 534.4 eV, corresponding to O′, Si−O_2, and Si−O−OH components. O′ has previously been assigned to a metastable amorphous phase, indicating the Si−O−Si bridge with a C−O−C bond or also a Si−O−C bond.[39,40] After the plasma process (Figure 7d), we observe a decrease in the peak corresponding to SiO_2 as well as a shift to lower binding energy (532.6 eV). Counter to this, we observe an increase in the peak O′ in addition to a shift to higher binding energy (531 eV). The C 1s spectra before CNT growth (Figure 7b) includes a C−C bond (sp2) at 284.8 eV, C−OH at 286.2 eV, and C═O at 287.6 eV due to surface impurities.[41] The appearance of peaks after growth located at 282.8, 283.7, and 289 eV can be assigned to SiC, amorphous SiC, and C═O−OH, respectively (Figure 7e).[42] XPS analysis and peak assignment in Figure 7c correspond to Si NCs dispersed in DI-water and sonicated for 60 min, as previously discussed (see Figure 2d and corresponding text). After the PECVD process (Figure 7f), the peak corresponding to Si^{4+} decreases in intensity and shifts to a higher binding energy by about 0.4 eV. The Si^{3+} component, which was not originally present in Figure 7c, is now observed at 103 eV also with the Si^{2+} component located at 102 eV; both peaks have shifted by about 0.4 eV compared to the expected BEs. The new peak located at 100.8 eV is assigned to SiC with the metallic Si peak located at 99.7 eV. These results suggest carbon atom diffusion through the oxide layer that forms intermediate bonding arrangements with silicon and oxygen atoms; this is supported by the appearance of peaks corresponding to O′ (Figure 7d) and C═O−OH (Figure 7e). Eventually some carbon also diffuses to the Si−SiO_2 interfaces of the Si NCs, forming a silicon carbide interlayer as confirmed by peaks corresponding to SiC (Figure 7e,f) and a-SiC (Figure 7e). The shifts of about 0.4 eV to higher binding energy also support the formation of a SiO_2/SiC interface.[43] Although reduced in intensity, the peak corresponding to metallic Si is still present in Figure 7d, confirming that a silicon core still remains. This would indicate that SiC is produced at the expense of our inner silicon nanocrystals.

Numerical Simulations of the Nucleation Mechanism. Let us now discuss the possible mechanisms and routes of CNT nucleation and growth on Si NCs in the microwave plasma environment. First, we should stress that tip-growth mode differs from that found in very similar experiments in the growth of carbon nanotubes on scratched silicon wafers.[44] In this case, the nanotubes were nucleated due to the small features on the hierarchically structured Si NCs surface, where the oxide has provided features with strain bonds versus relaxed H-terminated surfaces.[45] These features played the key role in nanotube formation. We propose the following main stages in the growth process (Figure 8). At the first stage of the process, the Si NCs are locally heated up by the plasma. After that, as a result of the carbo-thermal reduction of silicon oxide and locally increased temperature, the single graphene cap is formed and lifts the nanocrystal off the surface, thus initiating the tip-growth mode. Under such conditions, the Si NCs experiences

DOI: 10.1021/acsami.6b02599
ACS Appl. Mater. Interfaces 2016, 8, 19012−19023

strong ion flux due to localized irregularity of the electric field.[46] This in turn causes reshaping and formation of multiple steplike features on the Si NCs because of the thermal reorganization of silicon oxide to minimize the surface energy.

Simultaneously, partial carbon dissolution and saturation in the upper overheated layer leads to the nucleation of the next graphitic walls in the individual steps due to the minimization of adatom energy at the surface steps. To confirm this scenario, we have used numerical simulations by the diffusion-based model that was previously applied to similar systems.[47] Specifically, we have designed a randomized digital model of the system (oxidized Si NCs on the surface, Figure 9a) and calculated the pattern of electric field and adatom density profiles on the surface between the NCs under the typical deposition conditions. The direct purpose of the simulations was to calculate the fluxes to the individual oxidized Si NCs, so we used the diffusion equation in the form

$$\frac{\partial \xi}{\partial t} = D_S\left(\frac{\partial^2 \xi}{\partial x^2} + \frac{\partial^2 \xi}{\partial y^2}\right) + \Psi_+ - \Psi_- \tag{3}$$

where ξ is the density of adatoms on wafer surface, Ψ_+ represents the flux of carbon material to surface, and Ψ_- represents the carbon evaporation away from the substrate.[47] The diffusion coefficient can then be acquired:

$$D_S = \lambda^2 \nu_0 \exp(-\bar{\varepsilon}_d/kT_s) \tag{4}$$

where T_s is the substrate temperature, k is the Boltzmann's constant, λ is the crystal lattice parameter, and ν_0 is the frequency of oscillations in the crystal lattice.[47] The activation energy for atom diffusion on substrate surface, $\bar{\varepsilon}_d$, can be calculated by use of vectors $\mathfrak{R}$ and $\mathbf{N}$:

$$\bar{\varepsilon}_d = \frac{\mathfrak{R}\mathbf{N}}{\Theta\mathbf{N}} = \frac{\sum \varepsilon_k \eta_k}{\sum \eta_k} \tag{5}$$

where Θ is a unit vector, $\mathfrak{R}$ is vector of activation energies that are related to different surface features $\mathfrak{R}(\varepsilon_1, \varepsilon_2, ..., \varepsilon_k)$, and $\mathbf{N}$ is the density vector of surface features which were considered for the model surface $\mathbf{N}(\eta_1, \eta_2, ..., \eta_k)$.

To solve diffusion eq 3, we have simulated the electric field over substrate surface to model a shift in the diffusion activation energy caused by the interaction of adsorbed atoms with the near-surface electric field, accounting for the polarizability α of adsorbed atoms. In this instance, the resulting dipole moment $\tilde{P}$ of an adsorbed atom in the electric field $E(r)$ is $\tilde{P} = \tilde{p} + \alpha E$, where $\tilde{p}$ is the adatom dipole moment without electric field. The diffusion activation energy modified due to the presence of electric field becomes $\bar{\varepsilon}_{de} = \bar{\varepsilon}_d + W_e/kT$, and adatom acquires the energy in one jump across the lattice spacing λ:

$$W_e = \frac{\partial E}{\partial r}(\tilde{p} + \alpha E(r))\lambda \tag{6}$$

We neglected the electric charges present in the plasma-surface sheath and thus calculated the electric field near substrate surface using the Laplace equation $\Delta\varphi = 0$. A boundary condition of electric equipotentiality over the substrate surface exposed to plasma was also used. More details on the calculations and simulation of specific process can be found elsewhere.[47] The calculated electric field pattern (Figure 9b) in the model system demonstrates strong field strength near NC surfaces, but has much lower strength between the nanoparticles where the approximately equal charges of the various particles compensate each other. Stronger diffusion fluxes are ensured due to the effect of plasma, according to the calculation results. The calculated pattern of adsorbed atom density (Figure 9c) in the model system shows high density of adsorbed particles between the NCs and relatively low density near NC surfaces as a signature of strong fluxes from the surface to NCs. The direct result of the plasma effect is a more irregular pattern of material accumulated on the surface, resulting in stronger surface fluxes and faster saturation of nanoparticle surfaces with the carbon-containing material and eventually leading to supersaturation and nucleation of the nanotube caps on surface features and curved surfaces of silicon nanocrystals.

DISCUSSION

Let us now discuss some details of the carbon nanotubes nucleation and growth on the oxidized Si NCs. As it has been demonstrated, CNT growth has been achieved in our experiments using non-transition-metal catalyst. There have been numerous studies showing that metals that typically do not display catalytic activity can support CNT growth when in oxide form.[48−50] Mechanisms that facilitate growth of CNTs on oxide-based nonmetallic catalysts (e.g., SiO_2) are still not completely understood. However, there is some agreement that because of the high melting temperature of SiO_2 the typical vapor−liquid−solid (VLS) mechanism predicted during conventional CNT growth cannot take place.

It was confirmed through simulations on SiO_2 nanoparticles that a semisolid phase was absent during the VLS mechanism, permitting mechanisms such as vapor−solid−solid (VSS) or vapor−solid surface−solid (VSSS) to be suggested.[51] It is known that SiO_2 does not have the carbon solubility and catalytic function to decompose hydrocarbons, which is typical in metal catalysts used for CNT growth, although carbon solubility in metal catalysts such as Fe has been shown to be extremely sensitive to changes in temperature and catalyst size.[52] Indeed, the nucleation and growth of carbon nanotubes on nanosized SiO_2 particles was directly demonstrated in several experiments. In particular, it was shown that the silica nanoparticles with diameters less than 5 nm efficiently catalyzed the nucleation of single-walled carbon nanotubes.[53] Moreover, it has been demonstrated that the carbo-thermal reduction of CH_x on SiO_2 is restricted to the outer surface of SiO_2 nanoparticles. Such a localized carbon density is known to result in extended polyne chains that cover the surface layers of the SiO_2 particles and form amorphous silicon carbide.[54] The formation of this amorphous carbide layer can slow the diffusion rate of carbons into the SiO_2 layer. Hence, carbon supersaturation, a known prerequisite for CNT growth, seems unlikely to occur at the oxides subsurface. Nevertheless, during the reduction on SiO_2, simulations show that CO and H terminations are dissociated, leaving behind dangling bonds shown to encourage the continuance of CNT growth after formation of a SiC layer.[55] Owing to the increased curvature for smaller nanocrystals, it has also been hypothesized that strain at the nanocrystal surface could break and dissociate bonds among central atoms, therefore allowing further interaction with hydrocarbons.[48,56]

CNTs catalyzed on other metal oxides (i.e., different from SiO_2) have featured quite different growth patterns where the formation of a rolled-up graphitic appendage was needed to act as a template before turbostratic CNT growth could occur.[18] As a result of this high activation energy process, lower yields of

DOI: 10.1021/acsami.6b02599
ACS Appl. Mater. Interfaces 2016, 8, 19012−19023

CNT were produced compared with typical dissolution based growth mechanism.

CNT growth in our case has shown characteristic features originating from SiO_2 catalysts. Growth on silicon oxide differs from the growth based on other oxides and resembles more closely the typical growth observed from metallic catalysts.[17] In particular, we found that our NC catalysts were completely surrounded by a carbon shell exhibiting a tip-growth[57] (e.g., see Figure 6), which is typical in the growth induced by metal catalysts.

Silicon oxide has reduced catalytic properties compared to those of metal catalysts; therefore, plasma-induced partial decomposition of the hydrocarbons is necessary. The intrinsic chemical properties of silicon oxide contribute to the complete decomposition of the hydrocarbon radicals at the oxide surface.[37,39] The delivery of largely decomposed hydrocarbons and carbon atoms to the surface of the oxidized Si NCs also removes the need for high operating temperatures. Decomposed hydrocarbons and carbon atoms can be expected to adsorb first and then diffuse into the oxide; this is confirmed by our XPS analysis (Figure 7). However, the formation of a SiC interface as observed in our XPS measurements will eventually create a barrier and contribute to slowing down carbon diffusion through the oxide layer. Once carbon concentration at the oxide reaches solubility, precipitation of carbon forms a graphene island consisting of 5-membered rings, which act as a nucleation site for CNT growth. Therefore, similar to metallic-based growth, we believe that supersaturation and the formation of a graphitic cage are the steps that have allowed CNT growth as supported by TEM analysis.

It is possible that the nanoscale size of the oxidized Si NCs has an impact on the solubility of carbon atoms within the oxide because it has been observed for other nanoscale systems.[52] Also, the size of the catalysts may have played a role in reducing the melting temperature of the oxide shell. The small size of our particles coupled with the high-energy plasma could mean that our catalysts may be in a molten/liquid-like status at the surface as observed for VLS growth, where movement of Si and O atoms could create a space/hole or dislocation and facilitate the dissolution of already largely decomposed hydrocarbons. Carbon dissolution is also eased by this oxide, which is formed at ambient temperature during sonication. Oxide grown in this way presents strained bonds, which may also lead to defective arrangements and can enhance hydrocarbon radical capture, decomposition, and improve carbon solubility/diffusion. A high-energy strained surface is more likely on oxidized NCs versus H-terminated surfaces due to unconstrained bonding lengths in the latter case. Altogether, the oxidized surfaces offer suitable characteristics for presenting surface carbons and high solubility/diffusion. While we cannot confirm the exact intermediate states, our experimental evidence confirms the presence of carbon in the oxide layer and diffusion to the $Si-SiO_2$ interface.

The role of fragmentation has been shown to play an essential role in the preparation of our oxidized Si NCs catalysts. In particular, we have observed that the as-prepared micrometer-sized agglomerates (Figure 1a,b,d) had to be broken down into single Si NCs or submicrometer agglomerates (e.g., Figure 1e) before CNT growth could be observed. This requirement for small-sized agglomerates is beneficial to direct amorphous surface carbon into curved graphite and is consistent with the need for small catalysts in CNT growth activated by metal nanoparticles. Therefore, our oxidized Si NCs with high surface-to-volume ratio represent ideal templates for graphene cap formation and CNT growth. It is clear that the micrometer-sized agglomerates available in as-prepared samples are far too large to allow for the progression of any of the growth steps identified above, including carbon supersaturation and the formation of a suitably sized graphitic cage.

CNT growth was only successful on fragmented and oxidized Si NCs (T_{ox} > 1 nm), so the assumption can be made that the addition of an oxide shell further increases the adsorption of CH_x radicals. However, the role of the oxide thickness is more complex. In certain situations Si NCs with thin oxide layers have been unable to catalyze CNT growth. A thin oxide layer can certainly be expected to reach supersaturation much more quickly than a thicker oxide and therefore might lead to a high density of adsorbed carbon atoms very quickly with consequent poisoning of the catalyst surface. Bare Si NCs (e.g., H-terminated) might be unsuitable because of the nonsolubility of carbon in highly crystalline silicon at this temperature range and the possible formation of surface carbide. In other words, the oxide thickness has to be suitably matched to the flux of carbon atoms to allow for supersaturation in the oxide without excessive carbon adsorption/poisoning at the surface. This implies that the oxide thickness required for CNT growth is process-specific and cannot be generalized. At the same time, it suggests that it may be possible to grow CNTs on Si NCs with various degree of oxidation by adjusting the plasma process parameters.

CONCLUSIONS

We clearly demonstrated that the CNT growth directly from Si NCs is reliant on two main factors: nonagglomerated/small nanocrystal assemblies coupled with an oxide shell thickness of at least 1 nm. The critical amount of oxide along with the increased surface-to-volume ratio of nonagglomerated assemblies allows for the Si NCs to be used as a viable catalyst for the growth of CNTs. These factors clearly support the breakdown of hydrocarbons and/or the physisorption of already dissociated carbon atoms. Although synthesis directly from hydrogen terminated silicon does not appear to be a possibility, the necessary oxide thickness is thin enough for tunneling of carriers; therefore, we can imagine the construction of an ideal optoelectronic nanocomponent exhibiting unique quantum confinement properties.

EXPERIMENTAL SECTION

Silicon Nanocrystal Synthesis. Electrochemical etching of a boron doped p-type wafer (100), 0.1 Ω and 0.525 mm thickness, produced porous silicon that is mechanically pulverized to produce a powder containing agglomerated Si NCs. Hydrofluoric acid/ethanol (1:4) electrolyte was used, and current density equal to 1.52 mA cm^{-2} was sustained for 90 min.

Colloid Preparation. Around 1.5 mg of Si NCs were dispersed in both DI water and ethanol. Then, samples were sonicated for set time periods of 20, 40, and 60 min. The ultrasonication process promotes the fragmentation of large agglomerates and allows for a more controlled oxidation through surface exposure to the water-based oxidizing species.

Sample Preparation. Si NCs colloidal samples that were subjected to different fragmentation times (0 min, i.e., as-prepared, 20, 40, and 60 min) were then drop-cast (200 μL) on silicon substrate (1 cm^2) and left to dry.

PECVD Process. A 4 min pretreatment with N_2 plasma only (10 sccm) was included prior to the introduction of CH_4 (40 sccm) for a

DOI: 10.1021/acsami.6b02599
ACS Appl. Mater. Interfaces 2016, 8, 19012−19023

total growth time of 8 min. The operating pressure and temperature were 21 mbar and 600 °C, respectively.

ATR-FTIR. Attenuated total reflectance FTIR (ATR-FTIR) was measured using a Thermo-scientific spectrometer. Spectra were typically collected over a range of 600−4000 cm^{-1} at a 2 cm^{-1} resolution.

X-ray Photoelectron Spectroscopy. Chemical compostion was analyzed using an X-ray source (Al = 1486 eV) and the Kratos AxisUltra DLD spectrometer. Current and voltage were 10 mA and 15 kV, respectively, along with an operating pressure of 10^{-9} bar. Specific region scans (C 1s, O 1s, and Si 2p) were performed at a resolution of 0.05 eV and pass energy of 40 eV. Calibration of obtained spectra was performed using the C 1s peak located at 284.8 eV.

Scanning Electron Microscopy. A Hitachi S 4300 apparatus was used to capture images at 20 kV acceleration voltages and a working distance of 10 cm.

Transmission Electron Spectroscopy. For samples where CNT growth was detected, TEM analysis was performed using a JEOL 2100-F optical microscope at an acceleration voltage of 200 kV. Samples where CNTs were grown were mechanically detached and then transferred onto a carbon holey grid.

■ ASSOCIATED CONTENT

Supporting Information

The Supporting Information is available free of charge on the ACS Publications website at DOI: 10.1021/acsami.6b02599.

Photoluminescence and Fourier transform infrared spectroscopy of Si NCs as-prepared in DI water/ethanol and following fragmentation process (ultrasonication 20, 40, and 60 min), combined with detailed description of Si NCs surface effects (oxidation) on optical characteristics, and Raman spectroscopy of CNTs grown successfully from oxidized Si NCs (PDF)

■ AUTHOR INFORMATION

Corresponding Authors

*E-mail: rocks-c2@email.ulster.ac.uk.

*E-mail: mailto: D.Mariotti@ulster.ac.uk.

Notes

The authors declare no competing financial interest.

■ ACKNOWLEDGMENTS

This work has been partially funded by the Leverhulme Trust (IN-2012-136) and the EPSRC (EP/K022237/1, EP/M015211/1). C.R. would like to acknowledge the support for the Northern Ireland Department for Employment and Learning (DEL). This work was also partially supported by a NEDO Project (Japan). I.L. acknowledges the support from the School of Chemistry, Physics and Mechanical Engineering, Science and Engineering Faculty, Queensland University of Technology.

■ ABBREVIATIONS

CNTs, Carbon nanotubes
Si NCs, Silicon nanocrystals
Si, Silicon
C, Carbon
PECVD, Microwave plasma enhanced chemical vapor deposition
VLS, Vapor−liquid−solid
VSS, Vapor−solid−solid
VSSS, Vapor−solid surface−solid

■ REFERENCES

(1) Pavesi, L., Turan, R., Eds. *Silicon Nanocrystals: Fundamentals, Synthesis and Applications*; Wiley: Weinheim, Germany, 2010.

(2) Mangolini, L.; Thimsen, E.; Kortshagen, U. High-Yield Plasma Synthesis of Luminescent Silicon Nanocrystals. *Nano Lett.* **2005**, *5*, 655−659.

(3) Xu, Z.; Wang, D.; Guan, M.; Liu, X.; Yang, Y.; Wei, D.; Zhao, C.; Zhang, H. Photoluminescent Silicon Nanocrystal-Based Multifunctional Carrier for pH-Regulated Drug Delivery. *ACS Appl. Mater. Interfaces* **2012**, *4*, 3424−3431.

(4) Maier-Flaig, F.; Rinck, J.; Stephan, M.; Bocksrocker, T.; Bruns, M.; Kübel, C.; Powell, A. K.; Ozin, A.; Lemmer, U. Multicolor Silicon Light-Emitting Diodes. *Nano Lett.* **2013**, *13*, 475−480.

(5) O'Neill, A.; Bakirtzis, D.; Dixon, D. Polyamide 6/Graphene Composites: The Effect of in Situ Polymerisation on the Structure and Properties of Graphene Oxide and Reduced Graphene Oxide. *Eur. Polym. J.* **2014**, *59*, 353−362.

(6) Gao, F.; Viry, L.; Maugey, M.; Poulin, P.; Mano, N. Engineering Hybrid Nanotube Wires for High-Power Biofuel Cells. *Nat. Commun.* **2010**, *1*, 1−7.

(7) Zhu, Y.; Li, L.; Zhang, C.; Casillas, G.; Sun, Z.; Yan, Z.; Ruan, G.; Peng, Z.; Raji, A.-R. O.; Kittrell, C.; Hauge, R. H.; Tour, J. M. A Seamless Three-Dimensional Carbon Nanotube Graphene Hybrid Material. *Nat. Commun.* **2012**, *3*, 1225−1232.

(8) Takagi, D.; Hibino, H.; Suzuki, S.; Kobayashi, Y.; Homma, Y. Carbon Nanotube Growth from Semiconductor Nanoparticles. *Nano Lett.* **2007**, *7*, 2272−2275.

(9) Nakajima, A.; Fujii, D.; Uchino, M. Excellent Retention Characteristics of Nanocomposite Gate Insulator Consisting of Fullerene-Containing Polystyrene. *Appl. Phys. Lett.* **2013**, *103*, 013302−013304.

(10) Vilatela, J. J.; Eder, D. Nanocarbon Composites and Hybrids in Sustainability: A Review. *ChemSusChem* **2012**, *5*, 456−478.

(11) Ibrahim, I.; Bachmatiuk, A.; Warner, J. H.; Büchner, B.; Cuniberti, G.; Rümmeli, M. H. CVD-Grown Horizontally Aligned Single-Walled Carbon Nanotubes: Synthesis Routes and Growth Mechanisms. *Small* **2012**, *8*, 1973−1992.

(12) Hong, G.; Chen, Y.; Li, P.; Zhang, J. Controlling the Growth of Single-Walled Carbon Nanotubes on Surfaces Using Metal and Non-Metal Catalysts. *Carbon* **2012**, *50*, 2067−2082.

(13) Hu, S.; Rajamani, R.; Yu, X. Flexible Solid-State Paper Based Carbon Nanotube Supercapacitor. *Appl. Phys. Lett.* **2012**, *100*, 104103−104105.

(14) Švrček, V.; Mariotti, D.; Shibata, Y.; Kondo, M. A Hybrid Heterojunction Based on Fullerenes and Surfactant-Free, Self-Assembled, Closely Packed Silicon Nanocrystals. *J. Phys. D: Appl. Phys.* **2010**, *43*, 415402−415404.

(15) Evanoff, K.; Khan, J.; Balandin, A. A.; Magasinski, A.; Ready, W. J.; Fuller, T. F.; Yushin, G. Towards Ultrathick Battery Electrodes: Aligned Carbon Nanotube-Enabled Architecture. *Adv. Mater.* **2012**, *24*, 533−537.

(16) Hu, L.; Wu, H.; Gao, Y.; Cao, A.; Li, H.; McDough, J.; Xie, X.; Zhou, M.; Cui, Y. Silicon-Carbon Nanotube Coaxial Sponge as Li-Ion Anodes with High Areal Capacity. *Adv. Energy Mater.* **2011**, *1*, 523−527.

(17) Steiner, S. A.; Baumann, T. F.; Bayer, B. C.; Blume, R.; Worsley, M. A.; Moberlychan, W. J.; Shaw, E. L.; Schlögl, R.; Hart, A. J.; Hofmann, S.; Wardle, B. L. Nanoscale Zirconia as a Nonmetallic Catalyst for Graphitization of Carbon and Growth of Single- and Multiwall Carbon Nanotubes. *J. Am. Chem. Soc.* **2009**, *131*, 12144−12154.

(18) Kudo, A.; Steiner, S. A., III; Bayer, B. C.; Kidambi, P. R.; Hofmann, S.; Strano, M. S.; Wardle, B. L. CVD Growth of Carbon Nanostructures from Zirconia: mechanisms and a method for enhancing yield. *J. Am. Chem. Soc.* **2014**, *136*, 17808−17817.

(19) Rocks, C.; Mitra, S.; Macias-Montero, M.; Mariotti, D.; Svrcek, V. In *Carbon Nanomaterials Sourcebook: Vol. II*; Sattler, K. D., Ed.; CRC Press: Boca Raton, FL, 2016; pp 543−561.

DOI: 10.1021/acsami.6b02599
ACS Appl. Mater. Interfaces 2016, 8, 19012−19023

(20) Li, Q.; Yuan, D.; Guan, B.; Lin, Q.; Wang, X. Removal of Metal Catalyst in Multi-Walled Carbon Nanotubes with Combination of Air and Hydrogen Annealing Followed by Acid Treatment. *J. Nanosci. Nanotechnol.* **2008**, *8*, 5807−5812.
(21) Edwards, E. R.; Antunes, E. F.; Botelho, E. C.; Baldan, M. R.; Corat, E. Evaluation of Residual Iron in Carbon Nanotubes Purified by Acid Treatments. *Appl. Surf. Sci.* **2011**, *258*, 641−648.
(22) Kang, Z.; Tsang, C. H. A.; Wong, N.-B.; Zhang, Z.; Lee, S.-T. Silicon Quantum Dots: A General Photocatalyst for Reduction, Decomposition, and Selective Oxidation Reactions. *J. Am. Chem. Soc.* **2007**, *129*, 12090−12091.
(23) Švrček, V. Fabrication of Filled Carbon Nanotubes with Fresh Silicon Nanocrystals Produced In Situ by Nanosecond Pulsed Laser Processing in Environmentally Friendly Solutions. *J. Phys. Chem. C* **2008**, *112*, 13181−13186.
(24) Liu, M.; Lu, G.; Chen, J. Synthesis, Assembly, and Characterization of Si Nanocrystals and Si Nanocrystal-Carbon Nanotube Hybrid Structures. *Nanotechnology* **2008**, *19*, 265705−265709.
(25) Mariotti, D.; Švrček, V.; Mathur, A.; Dickinson, C.; Matsubara, K.; Kondo, M. Carbon Nanotube Growth Activated by Quantum-Confined Silicon Nanocrystals. *J. Phys. D: Appl. Phys.* **2013**, *46*, 122001−122003.
(26) Švrček, V. Ex Situ Prepared Si Nanocrystals Embedded in Silica Glass: Formation and Characterization. *J. Appl. Phys.* **2004**, *95*, 3158−3163.
(27) Merino, P.; Švec, M.; Martinez, J. I.; Jelinek, P.; Lacovig, P.; Dalmiglio, M.; Lizzit, S.; Soukiassian, P.; Cernicharo, J.; Martin-Gago, J. A. Graphene Etching on SiC Grains as a Path to Interstellar Polycyclic Aromatic Hydrocarbons Formation. *Nat. Commun.* **2014**, *5*, 3054.
(28) Kim, S.; Shin, D. H.; Choi, S.-H. Ultrafast Photoluminescence from Freestanding Si Nanocrystals. *Appl. Phys. Lett.* **2012**, *100*, 253103−253105.
(29) Švrček, V.; Mariotti, D.; Nagai, T.; Shibata, Y.; Turkevych, I.; Kondo, M. Photovoltaic Applications of Silicon Nanocrystal Based Nanostructures Induced by Nanosecond Laser Fragmentation in Liquid Media. *J. Phys. Chem. C* **2011**, *115*, 5084−5093.
(30) Lavine, J. M.; Sawan, S. P.; Shieh, Y. T.; Bellezza, A. J. Role of Si-H and Si-H2 in the Photoluminescence of Porous Si. *Appl. Phys. Lett.* **1993**, *62*, 1099−1101.
(31) Ogata, Y. H. Changes in the Environment of Hydrogen in Porous Silicon with Thermal Annealing. *J. Electrochem. Soc.* **1998**, *145*, 2439−2444.
(32) Cole, D. A.; Shallenberger, J. R.; Novak, S. W.; Moore, R. L.; Edgell, M. J.; Smith, S. P.; Hitzman, C. J.; Kirchhoff, J. F.; Principe, E.; Nieveen, W.; Huang, F. K.; Biswas, S.; Bleiler, R. J.; Jones, K. SiO2 Thickness Determination by X-Ray Photoelectron Spectroscopy, Auger Electron Spectroscopy, Secondary Ion Mass Spectrometry, Rutherford Backscattering, Transmission Electron Microscopy, and Ellipsometry. *J. Vac. Sci. Technol., B: Microelectron. Process. Phenom.* **2000**, *18*, 440−444.
(33) Shard, A. G. A Straightforward Method for Interpreting XPS Data from Core−Shell Nanoparticles. *J. Phys. Chem. C* **2012**, *116*, 16806−16813.
(34) Li, H.; Lusk, M. T.; Collins, R. T.; Wu, Z. Optimal Size Regime for Oxidation-Resistant Silicon Quantum Dots. *ACS Nano* **2012**, *6*, 9690−9699.
(35) Hofmeister, H.; Huisken, F.; Kohn, B. Lattice Contraction in Nanosized Silicon Particles Produced by Laser Pyrolysis of Silane. *Eur. Phys. J. D* **1999**, *9*, 137−140.
(36) Khalilov, U.; Pourtois, G.; van Duin, A. C. T.; Neyts, E. C. Self-Limiting Oxidation in Small-Diameter Si Nanowires. *Chem. Mater.* **2012**, *24*, 2141−2147.
(37) Büttner, C. C.; Zacharias, M. Retarded Oxidation of Si Nanowires. *Appl. Phys. Lett.* **2006**, *89*, 263106.
(38) Deal, B. E.; Grove, A. S. General Relationship for the Thermal Oxidation of Silicon. *J. Appl. Phys.* **1965**, *36*, 3770−3772.
(39) Thøgersen, A.; Selj, J. H.; Marstein, E. S. Oxidation Effects on Graded Porous Silicon Anti-Reflection Coatings. *J. Electrochem. Soc.* **2012**, *159*, D276−D281.
(40) Hijikata, Y.; Yaguchi, H.; Yoshikawa, M.; Yoshida, S. Composition Analysis of SiO 2/SiC Interfaces by Electron Spectroscopic Measurements Using Slope-Shaped Oxide Films. *Appl. Surf. Sci.* **2001**, *184*, 161−166.
(41) Hsiao, M.; Liao, S.; Yen, M.; Teng, C.; Lee, S.; Pu, N.; et al. Preparation and Properties of a Graphene Reinforced Nanocomposite Conducting Plate. *J. Mater. Chem.* **2010**, *20*, 8496−8505.
(42) Jiang, L.; Cheung, R.; Brown, R.; Mount, A. Inductively Coupled Plasma Etching of SiC in SF6/O2 and Etch-Induced Surface Chemical Bonding Modifications. *J. Appl. Phys.* **2003**, *93*, 1376−1383.
(43) Johansson, L. I.; Virojanadara, C.; Eickhoff, Th.; Drube, W. Properties of the SiO 2/SiC Interface Investigated by Angle Resolved Studies of the Si 2p and Si 1s Levels and the Si KLL Auger Transitions. *Surf. Sci.* **2003**, *529*, 515−526.
(44) Kumar, S.; Levchenko, I.; Ostrikov, K. K.; McLaughlin, J. A. Plasma-Enabled, Catalyst-Free Growth of Carbon Nanotubes on Mechanically-Written Si Features with Arbitrary Shape. *Carbon* **2012**, *50*, 325−329.
(45) Yang, S.; Li, W.; Cao, B.; Zeng, H.; Cai, W. Origin of Blue Emission from Silicon Nanoparticles: Direct Transition and Interface Recombination. *J. Phys. Chem. C* **2011**, *115*, 21056−21062.
(46) Levchenko, I.; Ostrikov, K. Carbon Saturation of Arrays of Ni Catalyst Nanoparticles of Different Size and Pattern Uniformity on a Silicon Substrate. *Nanotechnology* **2008**, *19*, 335703.
(47) Levchenko, I.; Ostrikov, K.; Mariotti, D.; Švrček, V. Self-Organized Carbon Connections Between Catalyst particles on a Silicon Surface Exposed to Atmospheric-Pressure Ar+ CH 4 Microplasmas. *Carbon* **2009**, *47*, 2379−2390.
(48) Rümmeli, M. H.; Schäffel, F.; Kramberger, C.; Gemming, T.; Bachmatiuk, A.; Kalenczuk, R. J.; Rellinghaus, B.; Büchner, B.; Pichler, T. Oxide-Driven Carbon Nanotube Growth in Supported Catalyst CVD. *J. Am. Chem. Soc.* **2007**, *129*, 15772−15773.
(49) Steiner, S. A., III; Baumann, T. F.; Bayer, B. C.; Blume, R.; Worsley, M. A.; MoberlyChan, W. J.; Shaw, E. L.; Schlögl, R.; Hart, A. J.; Hofmann, S.; Wardle, B. L. Nanoscale Zirconia as a Nonmetallic Catalyst for Graphitization of Carbon and Growth of Single-and Multiwall Carbon Nanotubes. *J. Am. Chem. Soc.* **2009**, *131*, 12144−12154.
(50) Kudo, A.; Steiner, S. A., III; Bayer, B. C.; Kidambi, P. R.; Hofmann, S.; Strano, M. S.; Wardle, B. L. CVD Growth of Carbon Nanostructures from Zirconia: Mechanisms and a Method for Enhancing Yield. *J. Am. Chem. Soc.* **2014**, *136*, 17808−17817.
(51) Page, A. J.; Chandrakumar, K. R. S.; Irle, S.; Morokuma, K. SWNT Nucleation from Carbon-Coated SiO2 Nanoparticles via a Vapor-Solid-Solid Mechanism. *J. Am. Chem. Soc.* **2011**, *133*, 621−628.
(52) Harutyunyan, A. R.; Awasthi, N.; Jiang, A.; Setyawan, W.; Mora, E.; Tokune, T.; Bolton, K.; Curtarolo, S. Reduced Carbon Solubility in Fe Nanoclusters and Implications for the Growth of Single-Walled Carbon Nanotubes. *Phys. Rev. Lett.* **2008**, *100*, 195502−195504.
(53) Huang, S.; Cai, Q.; Chen, J.; Qian, Y.; Zhang, L. Metal-Catalyst-Free Growth of Single-Walled Carbon Nanotubes on Substrates. *J. Am. Chem. Soc.* **2009**, *131*, 2094−2095.
(54) Bachmatiuk, A.; Börrnert, F.; Grobosch, M.; Schäffel, F.; Wolff, U.; Scott, A.; Zaka, M.; Warner, J. H.; Klingeler, R.; Knupfer, M.; Büchner, B.; Rümmeli, M. H. Investigating the Graphitization Mechanism of SiO2 Nanoparticles in Chemical Vapor Deposition. *ACS Nano* **2009**, *3*, 4098−4104.
(55) Demuynck, L.; Arnault, J. C.; Polini, R.; Le Normand, F. CVD Diamond Nucleation and Growth on Scratched and Virgin Si(100) Surfaces Investigated by in-Situ Electron Spectroscopy. *Surf. Sci.* **1997**, *377-379*, 871−875.
(56) Heidari Saani, M.; Ghodselahi, T.; Esfarjani, K. Strain-Induced Instability of Spherical Nanodiamond Hydrocarbons: Effect of Surface CH N and Charging. *Phys. Rev. B: Condens. Matter Mater. Phys.* **2009**, *79*, 125429−125436.

DOI: 10.1021/acsami.6b02599
ACS Appl. Mater. Interfaces 2016, 8, 19012−19023

(57) Bachmatiuk, A.; Börrnert, F.; Schäffel, F.; Zaka, M.; Martynkowa, G. S.; Placha, D.; Schönfelder, R.; Costa, P. M. F. J.; Ioannides, N.; Warner, J. H.; et al. The Formation of Stacked-Cup Carbon Nanotubes Using Chemical Vapor Deposition from Ethanol over Silica. *Carbon* **2010**, *48*, 3175−3181.

DOI: 10.1021/acsami.6b02599
ACS Appl. Mater. Interfaces 2016, 8, 19012−19023